Electromagnetic Simulation of RF Burn Injuries Occurring at Skin–Skin and Skin–Bore Wall Contact Points in an MRI Scanner with a Birdcage Coil

Minghui Tang, PhD[1], Kiyoi Okamoto, RT, BS[2], Takuya Haruyama, RT, MS[3], and Toru Yamamoto, PhD[1*]

[1] Division of Biomedical Engineering and Science, Faculty of Health Sciences, Hokkaido University, Sapporo, 060-0812, Japan

[2] Graduate School of Health Sciences, Hokkaido University, Sapporo, 060-0812, Japan

3 Department of Radiology, Hakodate Municipal Hospital, Hakodate, 041-8680, Japan

Corresponding author:

Toru Yamamoto

Faculty of Health Sciences, Hokkaido University

Kita 12 Nishi 5, Kita-ku, Sapporo, 060-0812 Japan

Tel: +81-11-706-3412

E-mail: yamamoto@hs.hokudai.ac.jp

Purpose: To simulate radiofrequency (RF) burns that frequently occur at skin–skin and skin–bore wall contact points.

Methods: RF burn injuries (thumb–thigh and elbow–bore wall contacts) that typically occur on the lateral side of the body during 1.5T magnetic resonance imaging (MRI) scans were simulated using a computational human model. The model was shifted to investigate the influence of the position of the patient in an MRI scanner. The specific absorption rate (SAR), electric field, and temperature were mapped.

Results: Regarding the contact points located near the edge of the birdcage transmission coil, under the allowable maximum RF power exposure i.e., the average whole-body SAR at the safety limit value (2 W/kg), the 10-g-tissue-averaged SAR (SAR_{10g}) at those points significantly increased for both the thumb–thigh (180 W/kg) and elbow–bore wall (48 W/kg) cases. Both values significantly exceeded the highest safety limit of the partial-body SAR (10 W/kg). The electric field, the square of which is proportional to SAR, was remarkably high near the edge of the birdcage transmission coil. The peak SAR_{10g} for each injury case was associated with contact-point peak temperatures that reached 52 ℃ at approximately 1 min following RF exposure onset; a 1-min period of exposure to this temperature causes a first-degree burn.

Conclusions: We demonstrated high heat generation in RF burn injury cases in silico. The RF heating occurring on the lateral side of the body was strongly dependent on the electric field distribution, which is dominantly determined by an RF transmission coil.

Keywords: magnetic resonance safety, radiofrequency burn, specific absorption rate, SAR, electromagnetic simulation

Highlights

- Simulations confirm potential increases in local SAR at different contact points.
- Worst-case local SAR can vary up to 480% depending on patient positioning.
- The positional dependence is mainly determined by intrinsic electric field distribution within the RF coil.

Introduction

Increases in the magnetic field strength of magnetic resonance imaging (MRI) scanners have been known to cause accidents to occur during MRI examinations, such as the adsorption of a ferromagnetic oxygen tank; these accidents have been attracting an increasing amount of attention [1]. Approximately half of all such accidents are related to radiofrequency (RF) burns. The Medicines and Healthcare Products Regulatory Agency of the United Kingdom reported that 42% of all MRI accidents that occurred between 1993 and 2014 were classified as RF burns [2]. The Food and Drug Administration (FDA) of the United States reported that 55% of the MRI accidents that occurred between 2008 and 2017 were RF burns [3]. The FDA data reveal that, among 906 thermal injury cases, including those not clearly related to RF burns, the most frequent cause of thermal injury was the skin–skin contact (147), followed by the contact with an MRI coil (138) and the bore wall (97) [3]. According to a Japanese survey reported in 2011, 12% of 1,319 hospitals had observed RF burn injuries [4]. The most frequent locations of these injuries were skin–skin contact points between calves (39 cases), followed by points of contact with the cables of various MRI components (38 cases), and, lastly, points of contact with the bore wall (12 cases). Theoretically, RF heating is proportional to the square of the static magnetic field strength of the MRI system; a retrospective study of previous questionnaire results showed that the rate at which patients perceived RF heating increased quadratically with increasing magnetic field strength [5]. Owing to the prevalence of 3T MRI scanners and the development of ≥ 7T MRI systems, the number of RF burn injuries has been increasing in recent decades, with the FDA reporting 419 cases between 1997 and 2009 [6], and 906 cases between 2008 and 2017 [3]. Thus, RF burn injuries represent an urgent problem that needs to be addressed to ensure patient safety.

A variety of studies have been performed in an attempt to understand the mechanism of RF burn injuries; to date, these studies have ranged from experimental research on metallic object-related RF heating to research focusing on patient posture. Dempsey et al. measured the RF-induced temperature of copper wires held by non-conductive materials [7]; they observed that the temperature of the wires became relatively high only under the resonant condition, i.e., a looped wire with a resonant capacitance, and a straight wire at resonant length. Because the temperature of a simple looped wire was not found to be hazardously high, the resonance of the induced current circuit that includes the looped or straight wire has been emphasized. This pilot study was performed for the metallic materials without the conductive human body. RF-induced temperatures were measured for implants that were embedded into a conductive gel phantom [8,9]. These researchers observed a substantial temperature increase at certain values of implant length suggesting that the antenna effect of the conductive wire at resonant length could be of particular concern for MRI examination of patients with implants. Furthermore, it is understood that, when a closed conductive loop is formed by the body and conductive objects, or because of the posture of the patient, the induced currents tend to concentrate at the body–implant or skin–skin contact points in the loop circuit, resulting in localized heating [10]. Reports from the United Kingdom [2] and Japan [4] identified the conductive loop as the main cause of RF burns due to it being associated with the highest number of injuries. In clinical practice, the formation of the conductive loop tends to be of utmost concern. However, it is difficult to use the loop formation to explain the injuries at the skin–bore wall contact points. Thus, the comprehensive mechanisms of RF burn injuries remain unknown.

The specific absorption rate (SAR) is a dosimetric parameter used to assess Joule heating due to RF power exposure; it can be defined as the amount of heat absorbed per unit mass of human tissue. The average SAR of a patient in an MRI scanner is estimated before a scan from the planned RF power and patient weight [11]. The International Electrotechnical Commission (IEC) has specified the upper limits of whole-body SAR (2 W/kg) and partial-body SAR (2–10 W/kg); the latter SAR value varies with the change in ratio between the RF-exposed patient mass and the total patient mass in a body coil [12]. These limits are intended to ensure that a safe temperature is maintained within the body under the conditions of normal operating mode (i.e., during clinical practice). Despite this safety precaution, the estimated SAR values that are averaged for the whole or part of the body may not provide information about the localized concentrations of induced RF eddy currents, which cause burn injuries. Precise evaluation of local SAR is crucial for understanding the mechanism of RF burn injuries and preventing them.

Finite-difference time-domain (FDTD) method-based computer simulations [13] have been performed to estimate the local SAR in a computational human model [14] under different RF frequency [15] and landmark position conditions [16]. Because the relationship between the SAR and temperature distribution is not straightforward [17], temperature simulations have also been performed [15,18,19] to meet the IEC standard for normal operating mode; this standard states that the body core temperature should not increase by more than 0.5 ℃. These types of computer simulation methods have been widely used for RF heating analysis [20–24], especially for cases involving implants [21–23,25,26], as they can be used to ensure MRI compatibility in terms of RF heating of medical implantable devices [27]. The computer simulations provide a convenient way to evaluate the local SAR and the aforementioned temperature increase; however, there are no computer-simulation-based studies that have focused on the most frequent RF burn injuries, which occur at skin–skin and skin–bore wall contact points. Furthermore, it has been reported that the arm placement of a patient in an MRI scanner influences the detectability of lesions in the liver [28], and that arm placement variation may cause skin–skin or skin–bore wall contact-related RF burn injuries [2–4]. Thus, in this study, we used MRI analysis-purposed electromagnetic analysis software to simulate RF burn injuries at different contact points (i.e., skin–skin contact between the thumb and skin of the thigh, and skin–bore wall contact at the elbow) on the lateral side of a human body in an MRI scanner with a birdcage coil.

Materials and methods

We used electromagnetic field analysis simulation software (Sim4Life Ver. 2.2, ZMT Zurich MedTech AG) to model two cases of RF burn injuries in silico on the anatomical human model Duke (age: 34 years, height: 1.80 m, weight: 72 kg, body mass index: 22.2 kg/m^2) [14] shown in Fig. 1. The injuries were located at two contact points, i.e., between the right thumb and skin of the thigh and between the right elbow and bore wall of the MRI system. The static magnetic field (B_0) of the MRI system was 1.5T (resonance frequency: 64 MHz), and the circular excitation RF transmission coil was built using the Sim4Life BCAGE tool [29]: a high-pass birdcage type with eight legs (length: 0.65 m) and a shield (length: 1.28 m, radius: 0.375 m). Eight phase-adjusted sources respectively fed currents to eight legs. The end-ring, with eight capacitances (7.2 pF), was designed as an octagon with a 0.315-m inner radius at both ends. The bore was designed as a cylinder (thickness: 5 mm) with a 0.288-m inner radius; it was made from fiber-reinforced plastics (conductivity: 1×10^{-14} S/m, relative permittivity: 5.5). The spatial resolution (i.e., voxel size) of the simulated model was $2 \times 2 \times 2$ mm^3.

Burn Injury Model for the Thumb–Thigh Contact Case

A 31-year-old male patient who complained of lumbar pain underwent a 1.5T MRI examination of the lumbar spine. After the examination, the patient reported local pain in his right hand, and a small, white, swollen area with a diameter of 3 mm was found on the skin. A third-degree burn was also found on the skin of the right lateral thigh [30]. We modeled this case by moving the bones of the right arm and right thigh of the human model to make a contact point between the right thumb and skin of the lateral thigh (Fig. 2(a)). The extent to which each bone was translated and rotated is detailed in Table 1. The resulting contact area was 32 voxels (128 mm^2).

Burn Injury Model for the Elbow–Bore Wall Contact Case

A 13-year-old male patient underwent a 1.5T MRI examination of the hip joint. During the examination, his arms were folded, and the right arm was in contact with the bore wall of the MRI scanner. A second-degree burn was subsequently found on the right elbow [31]. We modeled this case by moving the bones of both arms and hands of the human model to form a contact point between the right elbow and bore wall of the MRI scanner; the left elbow was positioned 31 mm away from the bore wall (Fig. 2(b)). The extent to which each bone was translated and rotated is detailed in Table 2. The resulting contact area was 1 voxel (4 mm^2).

SAR Simulation

Electromagnetic simulations were performed for each RF burn injury case model; the three-dimensional SAR distribution of both the averaged SAR for 10 g of tissue (SAR_{10g}) and unaveraged SAR of each voxel (SAR_v) were mapped on the human model. In this simulation, a continuous RF magnetic field (B_1) (100% duty cycle) with a magnitude of 1 μT at the center of the scanner was applied to yield the normalized SAR values [24]. The distribution of the electric field strength inside the scanner as well as the electric field of the empty scanner for reference were also mapped. All simulations for each RF burn injury case were first performed under the condition that the contact point lied on the central line of the transmission coil (white dotted line in Fig. 2). To investigate how the position of a patient in the MRI scanner affects the SAR distribution, Duke was shifted 140, 280, 330, 350, 420, and 700 mm in the direction of B_0, with the origin corresponding to the center of the transmission coil in each RF burn case. In the thumb–thigh and elbow–bore wall contact cases, Duke was shifted downward and upward, respectively (i.e., negative and positive directions, respectively, as shown in Fig. 2). The average SAR for the whole body (SAR_w) was calculated at every position in each case. To simulate the worst-case clinical scenario, the worst-case peak local SAR_{10g} values were normalized to a condition of 2 W/kg SAR_w which is the maximum allowable SAR_w in the normal operating mode [12]: multiplying 2/(simulated SAR_w) to the simulated SAR_{10g}.

Thermal Simulation

The human body temperature was simulated for 15 min of RF exposure at SAR_w = 2 W/kg for each RF burn injury case. The temperature maps for the contact points were obtained in 1-min intervals. The initial temperature of the human body was 37 ℃, and the ambient air temperature was 25 ℃. The Sim4Life thermodynamic solver tool (i.e., p-thermal) was used to simulate the temperature utilizing Pennes' bioheat equation [32] to determine the heat transfer through perfusion [33]. In this thermal simulation, the following skin parameters from the database of IT'IS foundation [34] were used: mass density (1109 kg/m^3), specific heat capacity (3390.5 J/(kg･K), thermal conductivity (0.37 W/(m･K), heat generation rate (1.65 W/kg), and heat transfer rate (perfusion) (106 ml/min/kg). The heat transfer coefficient at the air–skin boundary was set at a higher value of 5 W/(m^2･K) [35] to conservatively simulate the human body temperature increases.

Results

Regarding the thumb–thigh contact case results, SAR_v and SAR_{10g} peaked at 116 and 14.2

W/kg, respectively, when the model was shifted downward by 350 mm (Fig. 3(a) and (c)), thereby exhibiting the same positional dependence. In the elbow–bore wall contact case, SAR_v and SAR_{10g} peaked at 210 and 3.1 W/kg, respectively, when the model was shifted upward by 320 mm (Fig. 3(b) and (d)). The position of the maximum SAR_v voxel for the human model was the same for all model positions in each case. In particular, the elbow–bore wall contact induced a sharp peak in SAR_v. SAR_w (Fig. 3(e) and (f)) varied according to the shift distance, but the positional dependence differed from those of SAR_v and SAR_{10g}. Specifically, at the locations of the peak SAR_v values, the SAR_w values were quite low, at 0.16 and 0.13 W/kg for the thumb–thigh and elbow–bore wall contact cases (Fig. 3(e) and (f)), respectively. The worst-case SAR_{10g} values corresponding to the maximum SAR_w (2 W/kg) value for safe RF exposure are shown in Fig. 4. The values of worst-case SAR_{10g} peaked at around the edge of the transmission coil varying up to 150% and 480% from those at the center for the thumb–thigh and the elbow–bore wall contact cases, respectively. All of the worst-case SAR_{10g} values for the thumb–thigh contact case exceeded the highest safety limit of the partial-body SAR (10 W/kg) by a factor of 2.9 at shift distance 700 mm to 17.0 at shift distance 320 mm (Fig. 4(a)), whereas those for the elbow–bore wall contact case remarkably exceeded the limit at 320 mm above the center by a factor of 3.8 (Fig. 4(b)).

When the scanner was empty, a significantly stronger electric field was shown near the edge of the birdcage transmission coil (Fig. 5(a) and (b)). When the human model was placed inside the MRI scanner (Fig. 5(c) and (d)), the electric field was modulated by the presence of an electrically conductive subject. Although stronger electric fields were observed near the side elements (leg) of the birdcage transmission coil (Fig. 5(c)), a distinct high electric field pattern remained at the edge (ring) of the birdcage transmission coil. More specifically, the electric field was quite weak within the human model, but strongly modified around it (Fig. 5(c) and (d)). The electric field strengths at the locations of the peak SAR_v in the human body (Fig. 6(a) and (b)) were 529 and 833 V/m for the thumb–thigh and elbow–bore wall cases, respectively. Under the condition of an average whole-body SAR of 2 W/kg, the temperature at the peak SAR_v voxels respectively increased to 52 ℃ and 51 ℃ in the thumb–thigh and elbow–bore wall cases after 1 min of RF exposure. Accordingly, after 15 min of exposure, these temperatures respectively increased to 92 ℃ and 76 ℃ (Fig. 7). The temperatures of the surrounding skin surface areas also increased with increasing RF exposure duration (Fig. 8).

Discussion

The results of simulating RF burn injuries using a computational human model confirmed high heat generation at the contact points. The human model positions corresponding to the peak SAR_v and SAR_{10g} values (Fig. 3) did not significantly differ from the reported positions of the actual RF burn injury cases. The thumb–thigh contact burn injury occurred when the lumbar spine was scanned [30], and the elbow–bore wall contact burn injury occurred when the pelvis was scanned [31]. The sharp increase in peak SAR_v (Fig. 3(b, d)) as a function of shift distance significantly exceeded the moderate increase in the maximum SAR_{10g} (Fig. 3(a, c)) (Fig. 3), indicating point-like heating due to the concentration of large electric currents at the contact point. In the thumb–thigh contact case, the peak SAR_{10g} value exceeded the highest safety limit of the partial-body SAR (10 W/kg) (Fig. 3(c)); conversely, the SAR_w value was far below the safety limit (2 W/kg) (Fig. 3(e)). Moreover, in the worst-case scenario, where the model was exposed to the maximum RF power under the conditions of the SAR_w safety limit, the SAR_{10g} value substantially exceeded the safety limit at all locations (Fig. 4(a)). Thus, although the maximum SAR_{10g} value was observed near the edge of the birdcage coil, this RF burn injury could occur irrespective of the patient position with respect to the bore axis. Regarding the worst-case scenario results for the elbow–bore wall contact case, the SAR_{10g} value remarkably exceeded the safety limit near the edge of the birdcage coil (Fig. 4(b))—480% of the value at the center—thereby reflecting the strong positional dependence of SAR_{10g} in an MRI scanner. The SAR_w value, which reflects the human volume in the area exposed to the RF power (i.e., the RF loading by the patient), was also found to be dependent on the patient position (Fig. 3(e) and (f)); however, its positional dependence differed from that observed for the SAR_{10g} value in the elbow–bore wall contact case.

The positional dependence of SAR_{10g} is strongly influenced by the electric field distribution in the MRI scanner. The electric field generated by the birdcage coil in an empty

MRI scanner tends to be considerably high near the end-ring of the high-pass-type birdcage transmission coil, i.e., where the lumped ports and capacitors are located [36–38], as shown in Fig. 5(a) and (b). Setting a conductive human body in the scanner modulated the electric field distribution. Our results of the electric field map showed an increase in the electric field near the side elements (leg) of the high-pass-type birdcage transmission coil in the central coronal plane (Fig. 5(c)). In particular, a strong increase in the electric field on the human body and its surroundings was observed in the vicinity of the end-ring, where high electric fields occurred due to lump capacitances (arrows in Fig. 5(c) and (d)). These phenomena of electric field modulation could be explained by the polarization field that originates from the charged particles within the sample that are moved to the boundaries of the sample [39]. This electric field distribution would explain why the SAR_{10g} values were highest at the thumb–thigh and elbow–bore wall contact points that were close to the end-rings.

The electric field determines the SAR, which is the product of the conductivity and square of the electric field. Although the electric field distribution in the scanner with a patient can be theoretically derived by solving Maxwell's equation, it is significantly influenced by the intrinsic electric field of the RF transmission coil; for example, the strength of the electric field near the end-ring of the birdcage transmission coil. Apart from this influence, caution to prevent the loop formation [7,31] can be motivated through Faraday's law of induction, where the conductive tissues of the subject are exposed to an alternating magnetic field (B1). However, the RF burn that occurred at the elbow–bore wall contact point cannot be explained by loop formation. Nevertheless, the electric field distribution within the MRI scanner can explain the RF burn injury that occurred near the bore wall including the thumb–thigh contact point case.

At the location corresponding to the peak SAR_{10g} value for each RF burn case, our simulations yielded temperatures that exceeded 52 ℃ at approximately 1 min after the onset of RF exposure at the SAR_w limit corresponding to the normal mode of operation (Fig. 7). In a previous study, first-degree burns occurred within 1 min of heating at a temperature of at least 52 ℃ [40]. Because most clinical pulse sequences require a scan duration that lasts more than 2 min [5], burns may happen. Oh et al. reported that the simulation of the temperature increase in the forearm tends to result in an overestimation of approximately 25% [18]. Thus, in consideration of this overestimation, the temperatures that were predicted to cause first- and second-degree burns within a 1-min period of heating were changed to 57 ℃ and 61 ℃, respectively. These temperatures were reached within 3 min in both cases (Figs. 7 and 8(a) and (b)). Normal body MRI scans entail the implementation of various pulse sequences that last approximately 10 min [5]. Therefore, our results clearly showed the RF burn injury cases in silico.

This study has some limitations. First, the influence of the size of the contact point area was not investigated. Although our results showed lower SAR_{10g} values in the case of a smaller contact area (i.e., the peak SAR_{10g} for the elbow–bore wall contact case with a single voxel contact was clearly less than that with 32 contact voxels for the thumb–thigh contact case), further investigation is needed. Secondly, any small gap can act as a significant capacitance; thus, the influence of a gap at the RF burn area would be another subject to be investigated. Additionally, this study focused on performing simulations for MRI systems with a birdcage transmission coil. Thus, because the electromagnetic properties vary according to the transmission coil design [41–43], the values of SAR and patient position dependence would be different for a different design. In this study, we employed the octagonal design of the end-ring of the birdcage transmission coil in order to shorten the simulation time greatly [37]. This simplification of the coil design enables accurate electromagnetic field calculations with the FDTD algorithm while keeping the field and currents distributions expected from the circular coil [44]. Further simulation with the exact modeling of the transmission coil is warranted. Furthermore, because the simulated SAR is dependent on the human model [16,45], we should mention that the relevance of our results only extends to the Duke human model. However, previously reported evidence that the SAR for the child model increases with less distance from the end-ring [45] supports the findings of our study because we modeled the case of the 13-yr-old patient who suffered an RF burn injury at the elbow–bore wall contact point (as reported in [31]). The Pennes' bioheat equation [32] that was applied in our temperature simulation has some shortcomings as it did not account for aspects such as thermoregulation [46,47], but instead assumed a constant perfusion rate and blood temperature, which may be relevant when modeling longer exposure duration. Consequently, our simulated temperature results may be overestimated. Furthermore, there have been several studies that compare the results of phantom experiments and their corresponding FDTD simulations; the studies consequently yielded simulation uncertainties of 20% for the SAR [48]. Although our results indicated relative SAR increase that were considerably higher, further validation experiment would help in establishing the current level of the simulation uncertainty. The MRI guidelines of the Medicines and Healthcare Products Regulatory Agency [49] recommend the use of 1–2 cm thick foam pads to insulate the patient from cables, the bore and between limbs. Our preliminary study showed that an air gap of such thickness caused a drastic decrease in SAR (data are not shown here). Therefore, the foam pads could potentially prevent RF burn accidents; however, the proper thickness and material need to be simulated.

In conclusion, the substantial amount of heat generated in RF burn injury cases was demonstrated by the electromagnetic simulation with a birdcage transmission coil. We found that the RF heating occurring on the lateral side of the body is dependent on the electric field distribution inside the MRI scanner, which is dominantly determined by the RF transmission coil.

Funding:

This work was supported by a Strategic Promotion of Innovative Research and Development (S-Innovation) grant from the Japan Agency for Medical Research and Development (AMRD) [grant number 20im0502002h0309].

Conflict of Interest: The authors declare that they have no conflict of interest.

References

[1] Chaljub G, Kramer LA, Johnson RF, Johnson J, Singh H, Crow WN. Projectile cylinder accidents resulting from the presence of ferromagnetic nitrous oxide or oxygen tanks in the MR suite. Am J Roentgenol 2001;177:27–30. https://doi.org/10.2214/ajr.177.1.1770027.

[2] Grainger D. MHRA MRI safety guidance: Review of key changes and emerging issues, https://www.sor.org/system/files/article/201504/io_2015_lr.pdf; 2015:42–7 [accessed 15 Sep 2020].

[3] Delfino JG, Krainak DM, Flesher SA, Miller DL. MRI-related FDA adverse event reports: A 10-yr review. Med Phys 2019;46:5562–71. https://doi.org/10.1002/mp.13768.

[4] Doi T, Yamatani Y, Ueyama T, Nishiki S, Ogura A, Kawamitsu H, et al. An investigative report concerning safety and management in the magnetic resonance environment: there are more accidents than expected. Nihon Hoshasen Gijutsu Gakkai Zasshi 2011;67:895–904. https://doi.org/10.6009/jjrt.67.895.

[5] Yamaguchi T, Abe Y, Ichino Y, Satoh S, Masuda T, Kimura S, et al. Heating sensation in patients with and without spinal fixation devices during MRI examination at different magnetic field strengths. J Magn Reson Imaging 2019;49:525–33. https://doi.org/10.1002/jmri.26307.

[6] Hardy PT, Weil KM. A review of thermal MR injuries. Radiol Technol 2010;81:606–9.

[7] Dempsey MF, Condon B, Hadley DM. Investigation of the factors responsible for burns during MRI. J Magn Reson Imaging 2001;13:627–31. https://doi.org/10.1002/jmri.1088.

[8] Nordbeck P, Fidler F, Weiss I, Warmuth M, Friedrich MT, Ehses P, et al. Spatial distribution of RF-induced E-fields and implant heating in MRI. Magn Reson Med 2008;60:312–9. https://doi.org/10.1002/mrm.21475.

[9] Muranaka H, Horiguchi T, Ueda Y, Tanki N. Evaluation of RF heating due to various implants during MR procedures. Magn Reson Med Sci 2011;10:11–9. https://doi.org/10.2463/mrms.10.11.

[10] Dempsey MF, Condon B. Thermal injuries associated with MRI. Clin Radiol 2001;56:457–65. https://doi.org/10.1053/crad.2000.0688.

[11] Saba L. Image principles, neck, and the brain. 1st ed. Florida: CRC Press; 2016.

[12] International Electrotechnical Commission (IEC). IEC 60601-2-33: Medical electrical equipment – Part 2-33: Particular requirements for the basic safety and essential performance of magnetic resonance equipment for medical diagnosis; 2012.

[13] Kane Yee. Numerical solution of initial boundary value problems involving maxwell’s equations in isotropic media. IEEE Trans Antennas Propag 1966;14:302–7. https://doi.org/10.1109/TAP.1966.1138693.

[14] Christ A, Kainz W, Hahn EG, Honegger K, Zefferer M, Neufeld E, et al. The Virtual Family - Development of surface-based anatomical models of two adults and two children for dosimetric simulations. Phys Med Biol 2010;55:N23–38. https://doi.org/10.1088/0031-9155/55/2/N01.

[15] Wang Z, Lin JC, Mao W, Liu W, Smith MB, Collins CM. SAR and temperature: Simulations and comparison to regulatory limits for MRI. J Magn Reson Imaging 2007;26:437–41. https://doi.org/10.1002/jmri.20977.

[16] Yeo DTB, Wang Z, Loew W, Vogel MW, Hancu I. Local specific absorption rate in high-pass birdcage and transverse electromagnetic body coils for multiple human body models in clinical landmark positions at 3T. J Magn Reson Imaging 2011;33:1209–17. https://doi.org/10.1002/jmri.22544.

[17] Collins CM, Liu W, Wang J, Gruetter R, Vaughan JT, Ugurbil K, et al. Temperature and SAR calculations for a human head within volume and surface coils at 64 and 300 MHz. J Magn Reson Imaging 2004;19:650–6. https://doi.org/10.1002/jmri.20041.

[18] Oh S, Ryu YC, Carluccio G, Sica CT, Collins CM. Measurement of SAR-induced temperature increase in a phantom and in vivo with comparison to numerical simulation. Magn Reson Med 2014;71:1923–31. https://doi.org/10.1002/mrm.24820.

[19] Wang Z, Lin JC, Vaughan JT, Collins CM. Consideration of physiological response in numerical models of temperature during MRI of the human head. J Magn Reson Imaging 2008;28:1303–8. https://doi.org/10.1002/jmri.21556.

[20] Restivo MC, van den Berg CAT, van Lier ALHMW, Polders DL, Raaijmakers AJE, Luijten PR, et al. Local specific absorption rate in brain tumors at 7 tesla. Magn Reson Med 2016;75:381–9. https://doi.org/10.1002/mrm.25653.

[21] Powell J, Papadaki A, Hand J, Hart A, McRobbie D. Numerical simulation of SAR induced around Co-Cr-Mo hip prostheses in situ exposed to RF fields associated with 1.5 and 3 T MRI body coils. Magn Reson Med 2012;68:960–8. https://doi.org/10.1002/mrm.23304.

[22] Golestanirad L, Angelone LM, Iacono MI, Katnani H, Wald LL, Bonmassar G. Local SAR near deep brain stimulation (DBS) electrodes at 64 and 127 MHz: A simulation study of the effect of extracranial

loops. Magn Reson Med 2017;78:1558–65. https://doi.org/10.1002/mrm.26535.

[23] Guo R, Zheng J, Chen J. MRI RF-Induced heating in heterogeneous human body with implantable medical device. In: Halefoğlu AM (ed) High-resolution neuroimaging - basic physical principles and clinical applications, 1st edn. Rijeka: InTech; 2018. https://doi.org/10.5772/intechopen.71384.

[24] Malik SJ, Beqiri A, Price AN, Teixeira JN, Hand JW, Hajnal JV. Specific absorption rate in neonates undergoing magnetic resonance procedures at 1.5T and 3T. NMR Biomed 2015;28:344–52. https://doi.org/10.1002/nbm.3256.

[25] Ho HS. Safety of metallic implants in magnetic resonance imaging. J Magn Reson Imaging 2001;14:472–7. https://doi.org/10.1002/jmri.1209.

[26] Hadert N, Liu Q, Zylka W. Numerical examinations of simplified spondylodesis models concerning energy absorption in magnetic resonance imaging. Curr Dir Biomed Eng 2016;2:653–8. https://doi.org/10.1515/cdbme-2016-0143.

[27] International Organization for Standardization (ISO). ISO/TS 10974:2012: Assessment of the safety of magnetic resonance imaging for patients with an active implantable medical device; 2012.

[28] Takatsu Y, Shimada Y, Miyati T, Shiozaki T, Kyotani K. Influence of arm position and respiration technique during liver examinations on the detectability of mammary lesions. Radiol Phys Technol 2018;11:328–37. https://doi.org/10.1007/s12194-018-0463-4.

[29] The Pennsylvania State University, Center for NMR Research Software. https://research.med.psu.edu/departments/center-for-nmr-research/software/. [Accessed 15 Sep 2020]

[30] Eising EG, Hughes J, Nolte F, Jentzen W, Bockisch A. Burn injury by nuclear magnetic resonance imaging. Clin Imaging 2010;34:293–7. https://doi.org/10.1016/j.clinimag.2009.06.025.

[31] Yamazaki M, Yamada E, Kudou S, Higashida M. Study of a temperature rise in RF irradiation during MR imaging : measurements of local temperature using a loop phantom. Japanese J Radiol Technol 2005;61:1125–32. https://doi.org/10.6009/jjrt.KJ00003943073.

[32] Pennes HH. Analysis of tissue and arterial blood temperatures in the resting human forearm. J Appl Physiol 1948;1:93–122. https://doi.org/10.1152/jappl.1948.1.2.93.

[33] Sim4Life Application and Support Team. Sim4Life Reference Guide release 3.0. 2016.

[34] Hasgall PA, Di Gennaro F, Baumgartner C, Neufeld E, Lloyd B, Gosselin MC, et al. “IT’IS Database for thermal and electromagnetic parameters of biological tissues,” Version 4.0. 2018.

https://doi.org/10.13099/VIP21000-04-0.

[35] Colin J, Houdas Y. Experimental determination of coefficient of heat exchanges by convection of human body. J Appl Physiol 1967;22:31–8. https://doi.org/10.1152/jappl.1967.22.1.31.

[36] Murbach MJ. EMF Risk Assessment: exposure assessment and safety considerations in MRI and other environments (Doctoral dissertation); 2013. https://doi.org/10.3929/ethz-a-010080329.

[37] Liu Y, Shen J, Kainz W, Qian S, Wu W, Chen J. Numerical investigations of MRI RF field induced heating for external fixation devices. Biomed Eng Online 2013;12:12. https://doi.org/10.1186/1475-925X-12-12.

[38] Saniour I, Gaborit G, Duvillaret L, Perrier A, Saniour I, Gaborit G, et al. "Experimental and simulated distribution of the RF electrical field inside a birdcage coil," in *Proc. 25th Annu. Meet. Exhib. ISMRBM*, Honolulu, United States, 2017, pp. 2625.

[39] Park B, Rajan S, Collins C, Angelone L. Analysis of conservative and magnetically induced electric fields in a low-frequency birdcage coil. J Electromagn Anal Appl 2013;5:271-280. https://doi.org/10.4236/jemaa.2013.57043.

[40] Willamson C, Scholtz JR. Time-temperature relationships in thermal blister formation. J Invest Dermatol 1949;12:41–7. https://doi.org/10.1038/jid.1949.7.

[41] Ibrahim TS, Kangarlu A, Chakeress DW. Design and performance issues of RF coils utilized in ultra high field MRI: Experimental and numerical evaluations. IEEE Trans Biomed Eng 2005;52:1278–84. https://doi.org/10.1109/TBME.2005.847564.

[42] Kim YC, Kim HD, Yun BJ, Ahmad SF. A simple analytical solution for the designing of the birdcage RF coil used in NMR imaging applications. Appl Sci 2020;10:2242. https://doi.org/10.3390/app10072242.

[43] Lucano E, Liberti M, Mendoza GG, Lloyd T, Iacono MI, Apollonio F, et al. Assessing the electromagnetic fields generated by a radiofrequency MRI body coil at 64 MHz: Defeaturing versus accuracy. IEEE Trans Biomed Eng 2016;63:1591–601. https://doi.org/10.1109/TBME.2015.2506680.

[44] Ibrahim TS, Lee R, Baertlein BA, Yu Y, Robitaille PM. Computational analysis of the high pass birdcage resonator: finite difference time domain simulations for high-field MRI. Magn. Reson. Imaging. 2000;18:835-43. https://doi.org/10.1016/s0730-725x(00)00161-2.

[45] Murbach M, Neufeld E, Kainz W, Pruessmann KP, Kuster N. Whole-body and local RF absorption in human models as a function of anatomy and position within 1.5T MR body coil. Magn Reson Med

2014;71:839–45. https://doi.org/10.1002/mrm.24690.

[46] Wulff W. The energy conservation equation for living tissue. IEEE Trans Biomed Eng 1974;BME-21:494–5. https://doi.org/10.1109/TBME.1974.324342.

[47] Murbach M, Neufeld E, Capstick M, Kainz W, Brunner DO, Samaras T, et al. Thermal tissue damage model analyzed for different whole-body SAR and scan durations for standard MR body coils. Magn Reson Med 2014;71:421–31. https://doi.org/10.1002/mrm.24671.

[48] Neufeld E, Kühn S, Szekely G, Kuster N. Measurement, simulation and uncertainty assessment of implant heating during MRI. Phys Med Biol 2009;54:4151–69. https://doi.org/10.1088/0031-9155/54/13/012.

[49] Grainger D. MHRA Safety guidelines for magnetic resonance imaging equipment in clinical use. 2018.https://assets.publishing.service.gov.uk/government/uploads/system/uploads/attachment_data/file/476931/MRI_guidance_2015_-_4-02d1.pdf

Figure legends

Figure 1: Human model (Duke) applied in simulations performed on the Sim4Life. The octagonal prism (black dashed lines) represents the birdcage transmission coil elements, and the white arrow represents the direction of the static magnetic field (B_0).

Figure 2: Simulation models of the two MRI RF burn injury cases: thumb–thigh contact (a) and elbow–bore wall contact (b). The light gray rectangle shows the position of the bore on the centeral horizontal plane. The black dashed lines represent the birdcage transmission coil elements. The white dotted line indicates the center of the scanner. The human body model was shifted downward (a) and upward (b) by a maximum of 700 mm. The white arrows show the locations of the reported RF burns.

Figure 3: Maximum SAR_v (a, b), SAR_{10g} (c, d), and SAR_w (e, f) versus the shift distance for the thumb–thigh (a, c, e) and elbow–bore wall (b, d, f) contact cases; the results were obtained under the conditions of simulating standard, continuous 1-μT RF magnetic field exposure. The human body position corresponding to the peak SAR was 350 mm downward the coil center for the thumb–thigh contact case (g), and 320 mm upward the coil center) for elbow–bore wall contact case (h). The black dashed lines and white dotted lines represent the birdcage transmission coil elements and the centers of the coils, respectively. The white arrows show the locations of the reported RF burns.

Figure 4: Worst-case SAR_{10g} versus the shift distance for the thumb–thigh (a) and elbow–bore wall contact (b) cases; the results were obtained under the conditions of the maximum allowable SAR_w at normal operating mode (2 W/kg). These values were estimated by multiplying 2/(simulated SAR_w) times each data point shown in Fig. 3(c, d). The dashed lines represent the upper safe limit for the partial-body SAR_{10g} (10 W/kg) corresponding to the normal operating mode.

Figure 5: Electric field strength maps simulated under the conditions of standard, continuous

1-μT RF magnetic field exposure. Maps on the central horizontal plane (left column (a, c)) where includes the thumb–thigh contact point and the horizontal plane above 79 mm from the central one (right column (b, d)) where includes the elbow–bore wall contact point. The maps in the upper row (a, b) show the electric field strength distribution within the empty scanner; those in the lower row (c, d) show the electric field strength distribution when the peak values of SAR were observed at the contact points (white arrows). The red dashed lines represent the projection of the birdcage transmission coil elements onto the plane of each map. To improve the visualization of the electric field strength near the human model, the color index was scaled to a maximum of 2000 V/m.

Figure 6: Enlarged views of the electric field strength maps of the contact points. The maps show the electric field strength distribution when the peak values of SAR were observed at the thumb–thigh and (a) elbow–bore wall (b) contact points (corresponding to Fig. 5(c) and (d), respectively). The white arrows show the locations of the contact points, and the values in the maps correspond to the electric field strengths at the contact points. The green lines denote the surface of the human body model.

Figure 7: Increases in temperature at the peak SAR voxel with 15 min of RF exposure under an average whole-body SAR of 2 W/kg: thumb–thigh (a) and elbow–bore wall contact (b) cases.

Figure 8: Maps of skin surface temperature at 3 min (a, b), 4 min (c, d), and 5 min (e, f) for the thumb–thigh (a, c, e) and elbow–bore wall (b, d, f) contact cases. Temperatures above 52 ℃, i.e., the minimum temperature associated with a burn injury within 1 min of exposure, are mapped. Scale bar, 10 mm. The maximum value of each color index is the maximum temperature of each mapped area for visibility.

Table 1. Bone translation and rotation details for the thumb–thigh model (Fig. 2(a))

Bone	Translation (mm)			Rotation (°)		
	X	Y	Z	X	Y	Z
Right humerus	40.04	-153.96	664.46	-166.80	6.57	88.15
Right radius	-8.32	-200.54	344.31	-177.30	5.35	95.41
Right ulna	-32.20	-189.33	356.00	179.03	10.38	90.02
Right femur	14.46	-58.43	125.65	-176.90	11.17	90.79

Table 2. Bone translation and rotation details for the elbow–bore model (Fig. 2(b))

Bone	Translation (mm)			Rotation (°)		
	X	Y	Z	X	Y	Z
Right humerus	-33.91	-169.09	284.46	-169.66	19.87	166.62
Right radius	62.68	-230.21	12.22	105.40	-1.05	166.61
Right ulna	59.03	-248.23	-10.02	101.56	23.77	168.41
Right metacarpal	122.95	-16.87	-60.43	83.45	-3.45	-169.54
Left humerus	-38.48	166.99	302.84	-170.55	-18.46	-0.78
Left radius	65.82	204.00	30.75	104.07	10.39	5.76
Left ulna	60.06	221.17	8.80	101.21	-16.40	1.73
Left metacarpal	74.34	-15.86	-31.70	104.75	15.54	-19.10

Figure 1

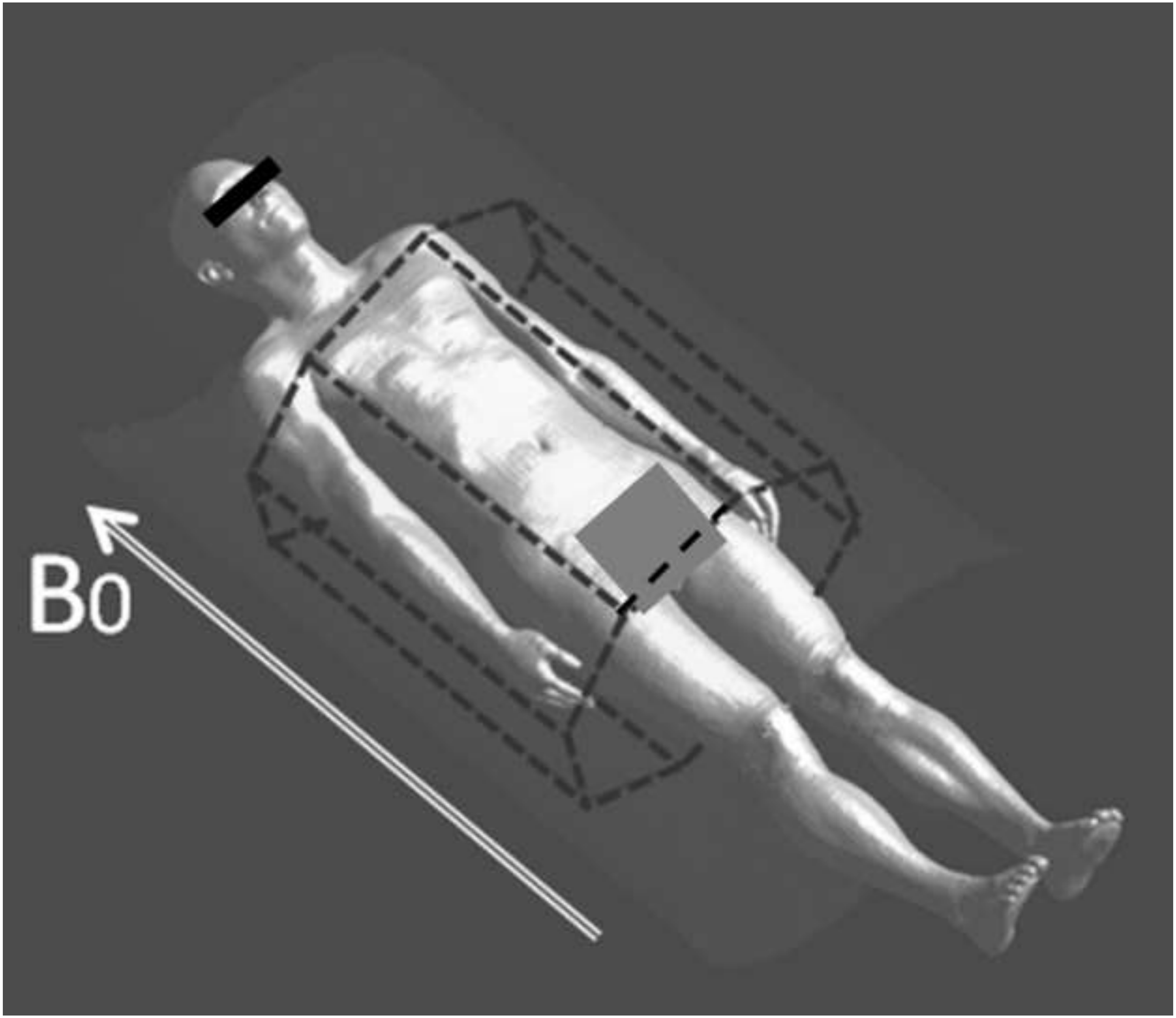

Figure 2

Click here to access/download;Figure;fig2.TIF

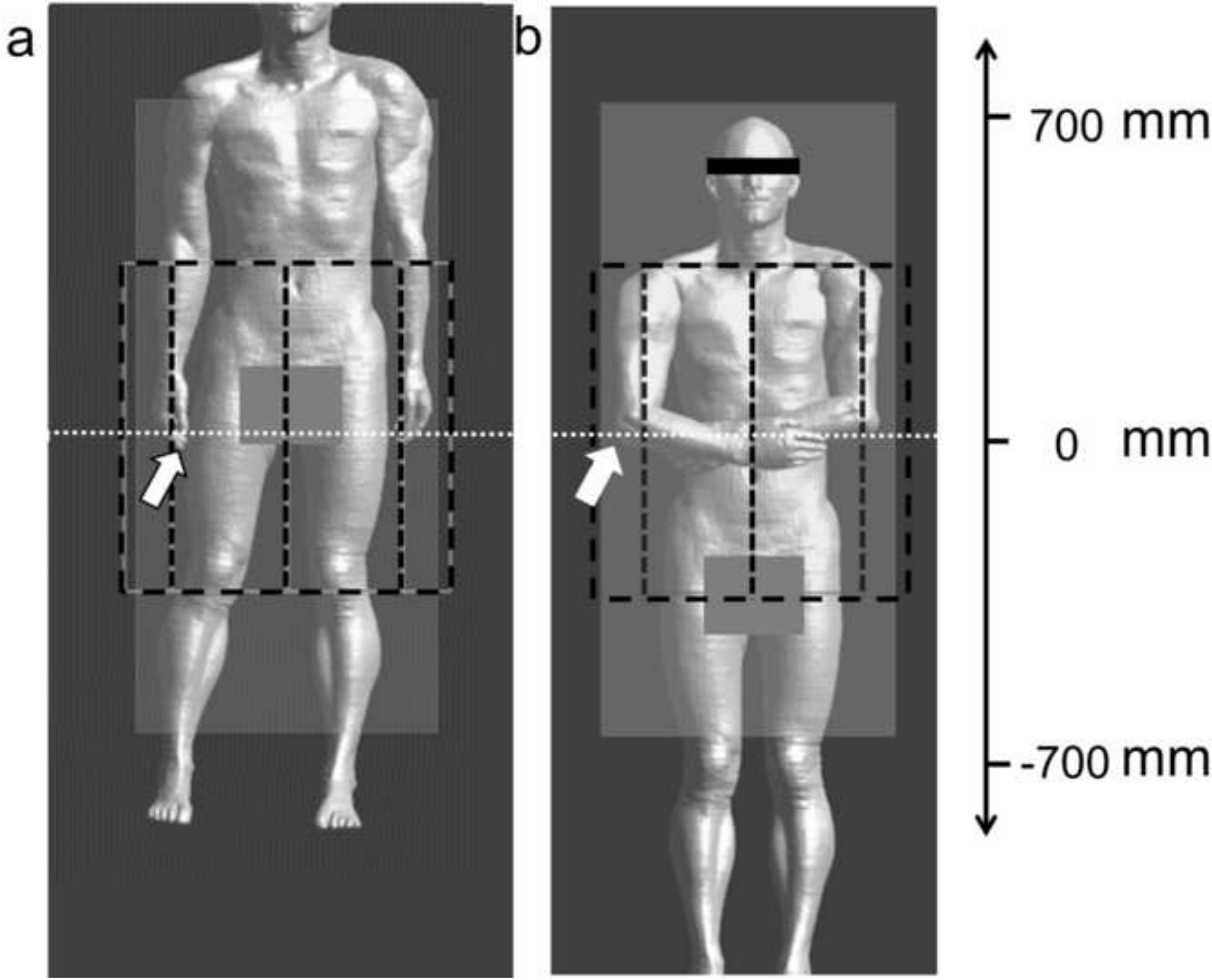

Figure 3

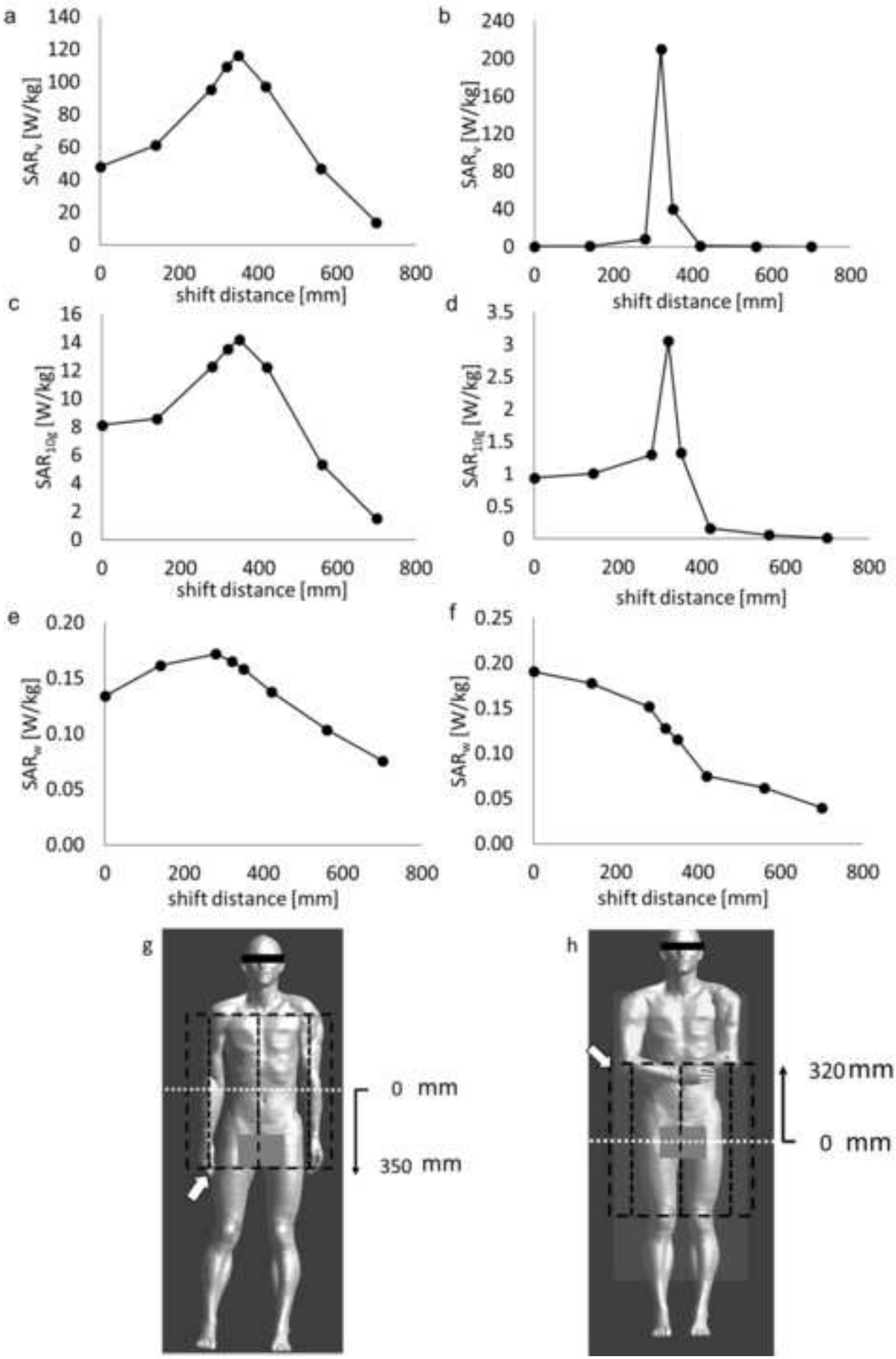
a
SAR$_v$ [W/kg]
shift distance [mm]
b
SAR$_v$ [W/kg]
shift distance [mm]
c
SAR$_{10g}$ [W/kg]
shift distance [mm]
d
SAR$_{10g}$ [W/kg]
shift distance [mm]
e
SAR$_w$ [W/kg]
shift distance [mm]
f
SAR$_w$ [W/kg]
shift distance [mm]
g
0 mm
350 mm
h
320 mm
0 mm

Figure 4

Click here to access/download;Figure;fig4.TIF

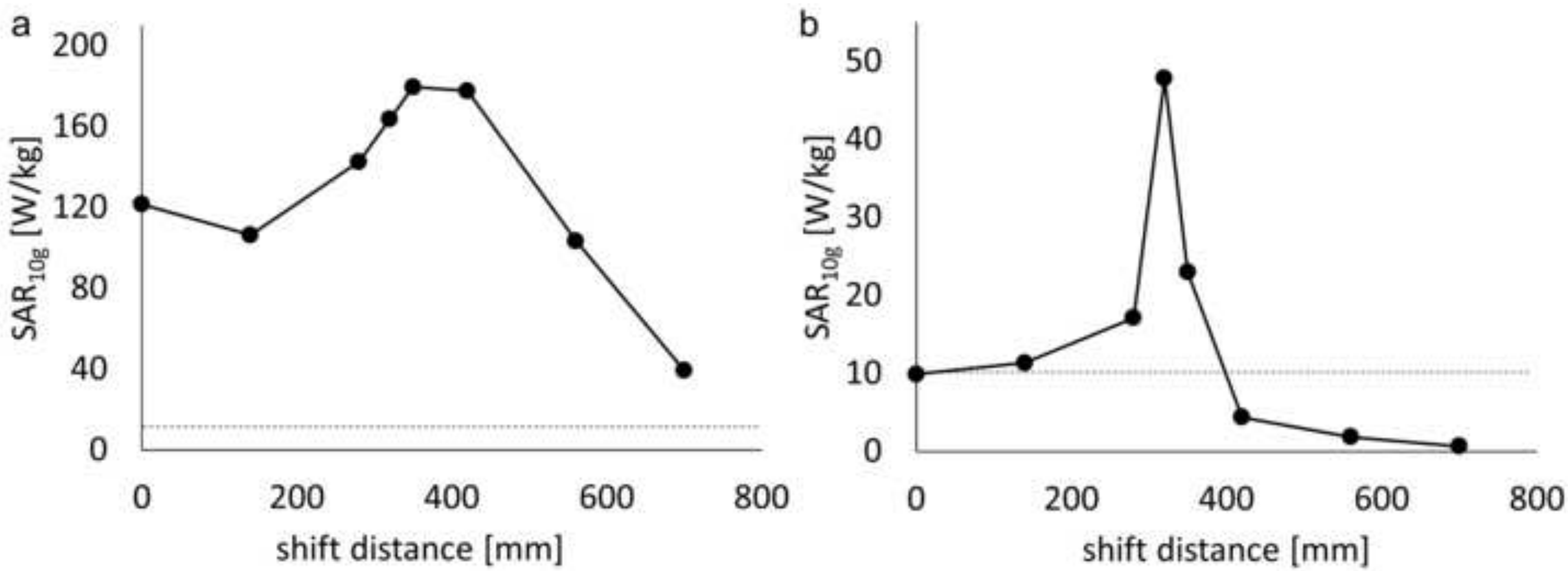

Figure 5

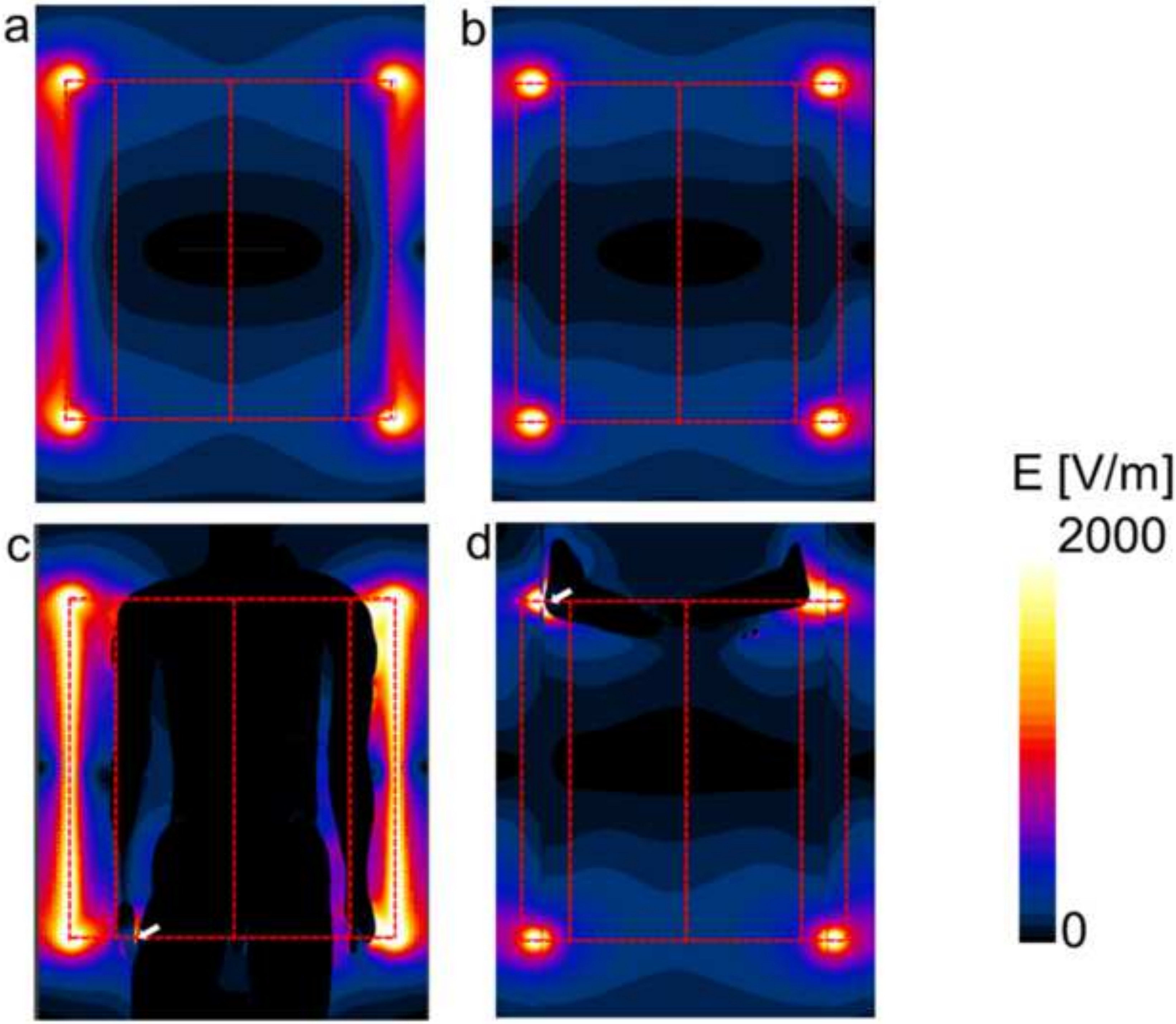

Figure 6

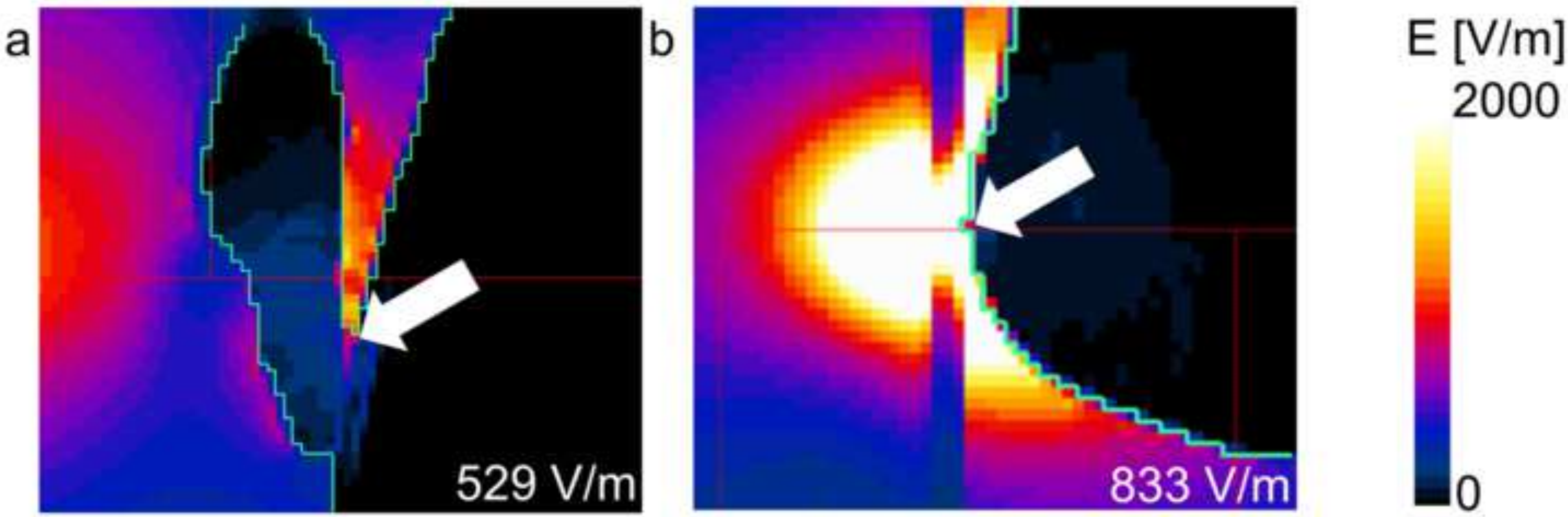

Figure 7

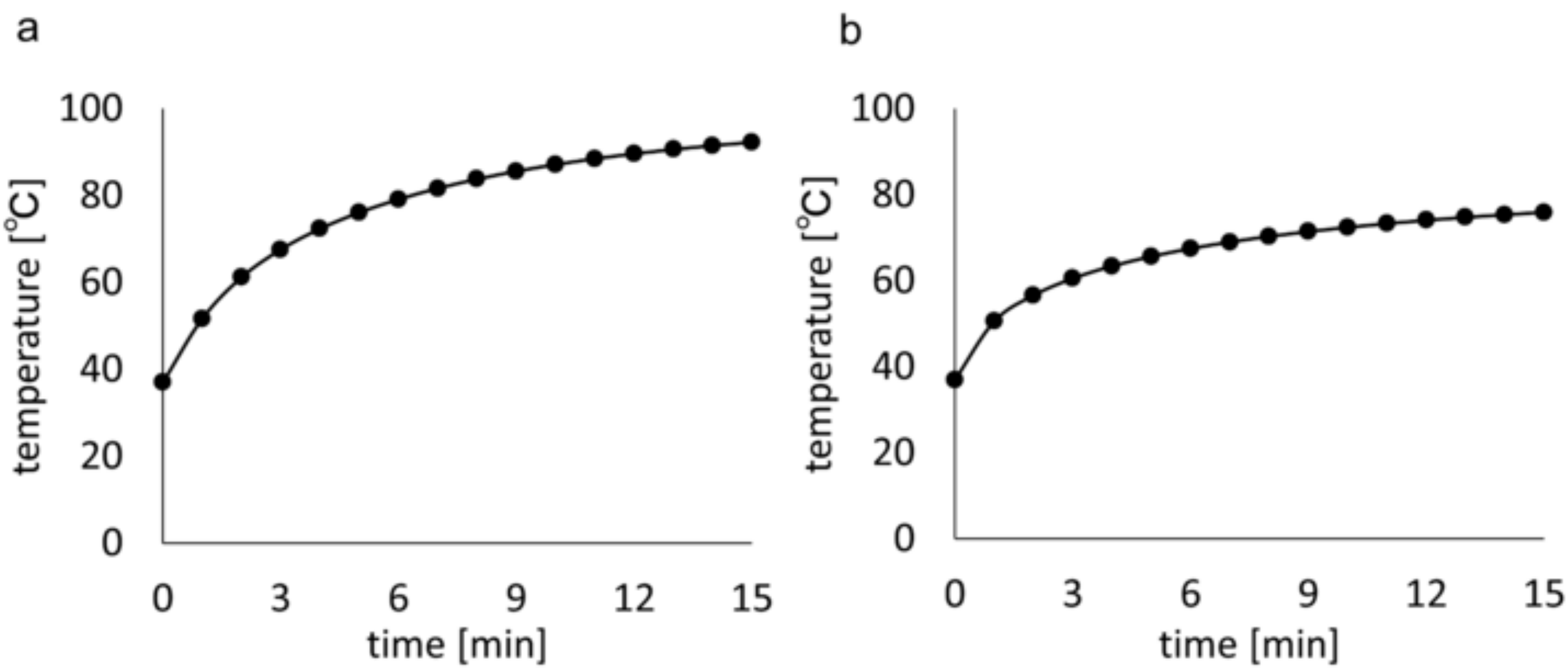
a
100
80
60
40
20
0
temperature [°C]
0
3
6
9
12
15
time [min]
b
100
80
60
40
20
0
temperature [°C]
0
3
6
9
12
15
time [min]

Figure 8 Click here to access/download;Figure;fig8.TIF